JOINT INSTITUTE FOR NUCLEAR RESEARCH
Flerov Laboratory of Nuclear Reactions

FINAL REPORT ON THE START PROGRAMME

Investigation of influence of a measurement chain on energy resolution of scintillator detectors

Supervisor:
Dr. Grzegorz Kaminski

Student:
Uri Carachure Gómez
Institute of Physics, National Autonomous University of Mexico (UNAM).

Participation period:
July 08 – August 15,
Summer Session 2025

Dubna, 2025

Investigation of influence of a measurement chain on energy resolution of scintillator detectors

Student: Uri Carachure Gómez[a]
Supervisor: Dr. Grzegorz Kaminski[b]
Co. Supevisor: Dr. Alexander Knyazev[b]
Co. Supevisor: MSc. Anh Mai[b]

[a] *Institute of Physics, National Autonomous University of Mexico (UNAM), Coyoacán, 04510, Mexico City, Mexico*
[b] *Joint Institute for Nuclear Research, Dubna, Russia.*

E-mail: carchure03@gmail.com

Abstract: This report presents the work carried out during a six-week stay in the START program at the sector 6, Flerov Laboratory of Nuclear Reactions, JINR. This work consists of three parts. The first part describes the coupling of the inorganic CsI(Tl) scintillators with the Hamamatsu R7600 photomultiplier tube (PMT). The second part addresses the measurement and comparison of two detectors of different lengths, 1" and 2" CsI(Tl), using the MBS acquisition system and the ^{22}Na and ^{60}Co sources. The third part presents the waveform acquisition using the PicoScope 6402D oscilloscope for the same sources and employing the 1" CsI(Tl) detector. Subsequently, using the same acquisition mechanism, measurements were made with a BC404 detector using ^{22}Na source. Finally, the computational analysis performed to obtain the spectra acquired with the MBS system and the PicoScope is presented, along with a discussion of the results.

Keywords: Scintillation detectors, organic and inorganic scintillators

Contents

1 Introduction

The Joint Institute for Nuclear Research (JINR) is an intergovernmental organization founded in 1956 in Dubna, Russia. Within JINR, the Flerov Laboratory of Nuclear Reactions (FLNR) conducts research including experiments on the synthesis and study of the physical and chemical nuclear properties of new superheavy elements; the study of fusion-fission reactions and multinucleon transfer in heavy-ion collisions; the analysis of the properties of nuclei at the limits of nucleon stability and the mechanisms of nuclear reactions with accelerated radioactive nuclei; and the study of heavy-ion interactions with various materials (polymers, semiconductors, electronic components for space technology, etc.) [1].

One of the principal fields of research at Flerov Laboratory of Nuclear Reactions is the Radioactive Ion Beam (RIB) research. ACCULINNA is one of the DRIBs (Dubna Radioactive Ion Beams) facilities and has been in operation since 1996. High intensity primary beams of ^{7}Li, ^{11}B, ^{13}C, ^{15}N and ^{18}O with energy values ranging between 32 and 50 AMeV are delivered by the $U-400M$

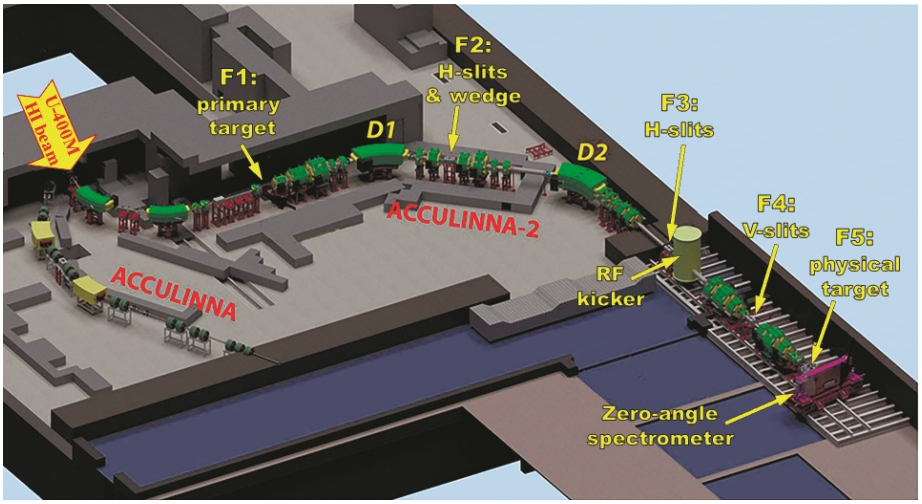

Figure 1: Separator ACCULINNA-2 in the Flerov Laboratory of Nuclear reactions, JINR Dubna

cyclotron to the production target of the separator. The secondary beams of ^{6}He and ^{8}He nuclei with energies of about 25 AMeV allowed us to gain new insights into the structure of neutron halo nuclei through the study of one- and two- neutron transfer reactions made with hydrogen and helium targets. Subsequently, the new ACCULINNA-2 fragment separator at the Flerov Laboratory of Nuclear Reactions (JINR, Dubna) [see Figure 1] entered its commissioning phase and began operations in early 2017. It is a 36 meters long achromatic separator consisting of two 45-degree dipole magnets, 14 quadrupoles, 8 multipoles (3 octupoles and 5 sextupoles) and 4 steering magnets. The high intensity primary beams are delivered by the $U-400M$ cyclotron to the rotating production target module installed in the first intermediate focal plane F1 to produce radioactive ion beams in fragmentation reactions via in-flight method [2].

Our research is to study the properties of light exotic nuclei, those with extreme proton-to-neutron imbalances near the limits of nuclear stability (drip lines). These nuclei are produced through nuclear reactions on light targets (for example deuterium) and radioactive ion beams (like $^{6,8}He$,^{9} Li,^{10,12} Be) generated by the ACCULINNA-2 fragment separator [3]. Currently, prominent examples of neutron-rich nuclei in question are ^{7}H, $^{10,12}He$, ^{10}Li which decay by emitting multiple neutrons. For that necessity, we need to detect charge particule in coincidence with neutron. We have a full set of charged particle detector telescopes. We have annular and square shaped single sided and double sided silicon strip detectors with thickness from 20 μm to 1.5 mm. The CsI(Tl) segmented arrays with square and annular shape are complementing well with corresponding Si telescopes. In addition, 40 neutron detection modules, based on stilbene crystals with corresponding PMTs are assembled into a neutron spectrometer was effectively used for a broad variety of experiments. In the future, we want to extend our efficiency of neutron detection with plastic scintillators. For that reason, first investigations of the detector properties of CsI(TI) and plastic BC404 are performed in this work.

1.1 Interactions of γ-rays with matter

Our detection system employs γ-ray sources for energy calibration purposes. The underlying detection mechanism relies on three primary interactions between γ-radiation and matter [4], which are analyzed in the following sections:

a) **Photoelectric effect**: Dominant interaction where the photon transfers all its energy to an atomic electron, ejecting it from the atom. The residual energy of the excited atom is released through:

- *Characteristic X-rays:* Electron reorganization in inner shells.
- *Auger electrons:* Emission of secondary electrons when energy is transferred to outer electrons.
- *Deposited energy:* $E_{e^-} = E_\gamma - E_b$ (E_b = electron binding energy).
- *Probability:* $\propto \frac{Z^n}{E_\gamma^{3.5}}$ ($4 \leq n \leq 5$), favored in heavy materials (Pb, NaI) and low energies.
- *Experimental signature:* Sharp peaks in spectra due to complete energy deposition.

b) **Compton scattering**: Quasi-elastic interaction where the photon transfers part of its energy to a loosely bound electron:

- *Relativistic kinematics:*

$$E'_\gamma = \frac{E_\gamma}{1 + \frac{E_\gamma}{m_e c^2}(1 - \cos\theta)}, \quad T_{\max} = \frac{2E_\gamma^2}{m_e c^2 + 2E_\gamma} \quad (\theta = 180^\circ)$$

- *Angular distribution:* High-energy photons prefer forward scattering ($\theta \approx 0^\circ$).
- *Detector manifestations:*
  - *Compton edge:* Maximum energy transferred to electrons.
  - *Backscatter peak:* Photons scattered at $\theta \approx 180^\circ$ ($E'_\gamma \approx 200 - 250$ keV).
  - *Compton continuum:* Energy distribution between 0 and $T_{\max}$.
- *Relevance in plastics:* Dominant process in organic scintillators (BC404) for $E_\gamma > 100$ keV.

c) **Pair production**: Energy-to-matter conversion when high-energy photons interact with nuclear fields:

- *Dual mechanism:*
  - Nuclear field (threshold $2m_e c^2 \approx 1.022$ MeV).
  - Electron field (threshold $4m_e c^2 \approx 2.044$ MeV).
- *Energy conservation:* $K_{e^-} + K_{e^+} = E_\gamma - 2m_e c^2$.

In figure 2 you can see a graph of the 3 different effects of matter radiation. On the X axis you can see that for energies less than 1 MeV, the dominant effect is the photoelectric effect, for energies from 1 to 5 MeV, the Compton scattering effect predominates and for energies greater than 5 MeV, the most dominant is the pair production. For the Y axis, we have the dependence of the atomic number (Z) of the absorbing material. In the energy region of our calibration sources, Compton scattering is even more dominant for materials with small Z like BC404, while for materials with a large Z like CsI(Tl) photoelectric effect becomes more probable.

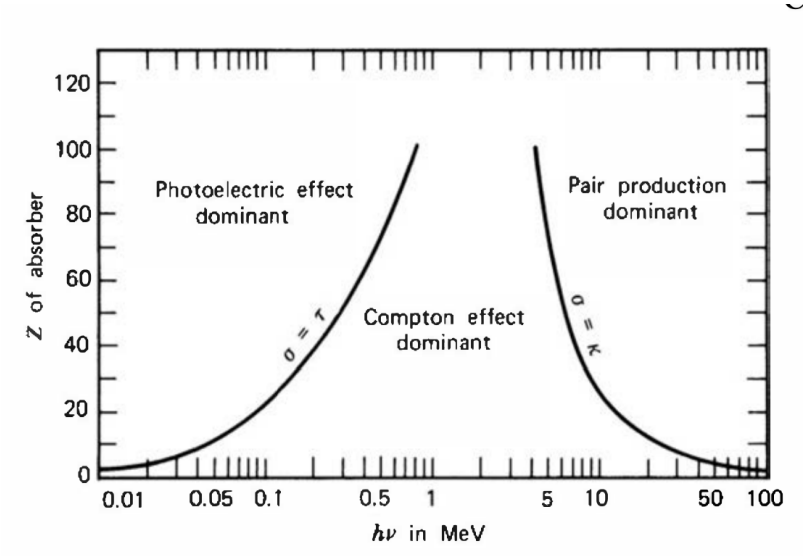

Figure 2: Dominant effect with respect to the energy and number of protons in the material [4]

1.2 Organic and inorganic scintillators

In experiments such as those carried out in ACCULINA-2, the secondary beam produced by the fragment separator impinged on a secondary target, will in turn generate reaction products such as charged particles, γ rays or neutrons, which have different detection mechanisms due to their nature, which is why the different properties of scintillator materials are used for their detection. In our case, we use scintillators such as CsI(TI) for charged particles and BC404 for neutrons, since the study of these helps us confirm theoretical models formulated for the reaction proposed for study or discover new properties of the nuclei, among others.

Scintillation detectors are devices for particle detection that take advantage of the optical properties of the material, since when impacted by a nuclear particle or radiation, they emit a flash of light. When coupled to an amplification device, such as photomultiplier tubes (PMTs), which behave linearly, these flashes can be converted into electrical pulses that can later be analyzed and counted electronically. The most relevant characteristics of scintillators are:

- *Energy linearity:* The response of scintillator detectors is linear with respect to the energy deposited from electrons; that is, the light output is linearly proportional to the excitation energy.

- *Time response:* The organic scintillator has a faster response time compared to the organic scintillator. This characteristic is why it is used for fast timing applications, such as time-of-flight measurement.

- *Pulse shape discrimination:* In some scintillators, it is possible to distinguish between different types of particles by analyzing the shape of the emitted light pulses, due to the excitation of fluorescence mechanisms caused by particles with different ionizing powers.

Organic scintillators are mainly composed of hydrocarbons containing linked or condensed benzene ring structures. Their most distinctive characteristic is the extremely fast decay time, on the order of nanoseconds, see example of BC404 in Table 1. In these scintillators, the scintillation light is produced from electronic transitions between valence states of the free molecules. The ground state corresponds to a singlet S_0, above which are the excited states $S^*, S^{**}, \ldots$, as well as the triplet state T_0 with its excited states $T^*, T^{**}, \ldots$. These levels correspond to excited vibrational modes of the molecule, with typical energy separations on the order of tenths of eV.

Inorganic scintillators are generally composed of ionic crystals, such as alkali halides (e.g., NaI, CsI) doped with activator impurities like Tl. The light emission mechanism in these materials is based on electronic processes that occur in the crystal lattice. The dopant introduces discrete energy levels within the forbidden band, allowing electrons excited from the valence band to the conduction band to relax through these levels, emitting photons in the visible range.

Unlike organic scintillators, where transitions occur between discrete molecular levels, in inorganic scintillators, energy bands and localized activation centers are involved. These materials typically exhibit longer decay times (on the order of hundreds to thousands of nanoseconds) and high density, which increases the probability of photoelectric interaction and, therefore, their efficiency in detecting high-energy γ radiation.

In this work, studies are carried out with BC404 and CsI(Tl) whose optical and material properties are found in the table 1, as well as the main applications given to each of these.

Property	**CsI(Tl)**	**BC-404**
Density (g/cm^3)	4.51	1.03
Refractive index (n)	1.788	1.58
Melting point (°C)	620	~70 (softening)
Light output (% of anthracene)	95	68
Decay time (ns)	1100	1.8
Emission wavelength (nm)	580	408
H/C ratio	N/A	1.10
Main applications	Heavy particles, γ (PSD)	Fast α, β detection,
fast counting, γ-rays		

Table 1: Physical, optical, and detection properties of the CsI(Tl) and BC-404 scintillators [5], [6].

1.3 Calibration and energy resolution

In this work, our aim is to thoroughly understand and quantify the performance of the scintillation detectors (organic and inorganic scintillators). The first step is to calibrate the amplitude and then observe the energy resolution by using a Gaussian function superimposed on a linear background.

Since the relationship between the electron pulses generated by scintillation light emission is linear for energies above 0.125 MeV, we can relate the detection channels from the electron pulses of the data acquisition system to the deposited energy of the particles and perform a linear fit as in equation 1.1. [4].

$$Energy = a * Channel + b \tag{1.1}$$

where a, b are the fitting parameters of the straight line.

For the case presented with the CsI(TI) scintillator where the photoelectric effect predominates, a shape adjustment is used the equation 1.2

$$f(x) = Ae^{-\left(\frac{x-\mu}{2\sigma}\right)^2} + Bx + C \tag{1.2}$$

where A corresponds to the amplitude of the Gaussian bell, μ is the centroid or mean value, σ represents the standard deviation, B is the slope of the linear background, and C is the intercept of the background.

The most relevant parameter is μ, as it allows us to identify events produced by charged particles and γ rays. Additionally, when calibrated with well-known radioactive sources, this value helps us determine the energy corresponding to each event.

For organic detectors like the BC-404, Gaussian fits are not possible due to the predominance of the Compton effect in the spectrum. For this reason, the calibration procedure is performed by fitting with the Fermi equation 1.3, which adequately adjusts the energy distribution of the effect.

$$E(x) = \frac{A}{1 + e^{-k(x-B)}} + C \tag{1.3}$$

where A, k, and C are fitting parameters, and B corresponds to the position of the Compton edge in the data fit.

The detector resolution is a key measure indicating the system's ability to distinguish between close energies. It is commonly defined as the relative width of the Gaussian peak in the histogram and is usually expressed as the percentage ratio of the full width at half maximum (FWHM) to the centroid:

$$R = \frac{\text{FWHM}}{\mu} \times 100\% \approx \frac{2.355\,\sigma}{\mu} \times 100\% \tag{1.4}$$

where μ is the peak centroid and σ the standard deviation obtained from the Gaussian fit. The FWHM (Full Width at Half Maximum) is the full width at half of the peak's maximum height.

A lower resolution implies that the detector can better distinguish between events with similar energies, which is crucial in experiments requiring precise particle or radiation identification.

In practice, the resolution depends on several factors, including the intrinsic characteristics of the detector, the acquisition electronics, and the noise present in the signal.

The dependence of energy resolution on energy deposit can be described with the nonlinear equation given by the equation 1.5.

$$R[\%] = \sqrt{A^2 + \frac{B^2}{E}} + C \tag{1.5}$$

where A, B and C are parameters describing the energy resolution behavior for the scintillator.

2 Methodology

This section describes three main aspects: (1) the coupling of the CsI(Tl) detector to the photomultiplier, (2) the measurements performed with the MBS system, and (3) the measurements carried out with the PicoScope equipment for the CsI(Tl) and BC404 scintillators.

2.1 Coupling

For the development of this part, it was necessary to lap two CsI(Tl) scintillation detectors with lengths of 1" and 2". With the aim of reducing noise, specific procedures and techniques for this type of material were applied.

The process requires a flat reference base (a glass plate), No. 1500 wet sandpaper with trimmed edges to minimize torsion, 95% concentration alcohol, latex gloves, and cotton.

The procedure consisted of wetting the sandpaper with alcohol and placing it parallel to the glass plate, holding it by hand. Since the crystal is a relatively soft but heavy material, lapping was done by taking advantage of its own weight, moving the detector slowly over the sandpaper without applying additional finger pressure to avoid unevenness or indentations on the surface [see Figures 3a and 3b].

Periodically, the lapping status was checked. For this, the surface was cleaned in three steps: (1) with a first dry cotton ball, the excess material was removed, (2) with a second cotton ball moistened with alcohol, the lapped surface was cleaned, and (3) with a third dry cotton ball, the remaining moisture was eliminated.

The process was considered complete when the following conditions were met: — Optical and tactile uniformity, — Absence of marked edges, — Elimination of visible reliefs or indentations.

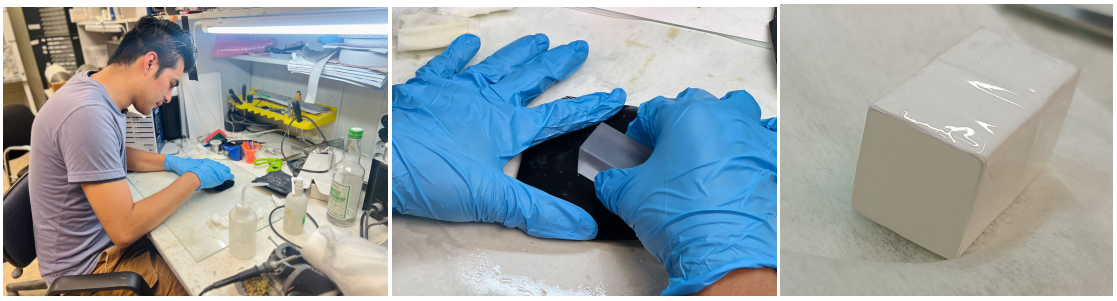

(a) Lapping the scintillator. (b) Lapping process. (c) CsI(Tl) detector with coating.

Figure 3: Scintillator preparation process: (a) lapping, (b) intermediate procedure, and (c) final coating.

After lapping the surfaces of the scintillator, five of its surfaces were coated with white PTFE tape in order to optimize the diffuse reflection of photons and provide hygroscopic protection. The remaining face, intended for coupling with the photomultiplier tube (PMT), was left uncovered. The assembly was secured with transparent tape (commonly known as *diurex*), used as a mechanical safety layer and for additional sealing [see Figure 3c].

The coupling with the Hamamatsu PMT model R7600, with dimensions 30 mm × 30 mm (square cross-section), is a procedure that requires patience and care, as it directly influences system performance and noise reduction. Since the refractive index varies from the scintillator to the detector, optical grease with an index close to $n \approx 1.5$ is used, which helps minimize internal reflection losses and maximize light transmission, in contrast to air, which has an index close to $n \approx 1$.

During the coupling, it is essential to avoid air bubbles. To achieve this, a drop of optical grease is placed in the center of the uncovered scintillator face, and then the PMT is positioned while making small circular movements and applying uniform pressure. The process continues until the grease is observed to be evenly distributed and starts to emerge from the edges.

Once the assembly is fixed, four of its sides are stabilized with insulating tape. Finally, the entire setup is wrapped with black insulating tape, both to mechanically secure the coupling and to protect it from external visible light.

2.2 Data Acquisition

2.2.1 Multi Branch System (MBS)

To perform a precise and efficient analysis of the signals generated by the scintillator and coupled to the photomultiplier, it is necessary to have a data acquisition system that allows their digitization, classification, and real-time storage.

In this context, the *Multi Branch System* (MBS) constitutes a flexible and high-performance platform for data acquisition in nuclear and particle physics experiments. This system is designed to handle multiple parallel data streams (*branches*), allowing simultaneous reading of various detectors or subsystems, as well as precise temporal synchronization of the recorded events [7].

To initiate the data acquisition process, the detector power supply (red cable) was connected to the CAEN SY4527 unit, responsible for providing high voltage, controlled via Geco software (General Control Software). The PMT coupled to the CsI(Tl) scintillator operated at 750 V with a current of 280 μA.
Initial connections were made to the oscilloscope to detect signals from radioactive sources (^{60}Co and ^{22}Na), with input impedance set to 50Ω. Subsequently, signals were connected in parallel to:

- The oscilloscope (impedance changed to 10 $M\Omega$)
- The amplifier and integrator MSCF-16-PMT

Detector outputs are shown as red and blue signals, while the integrated signal from one detector appears in green. The trigger generated by the LeCroy 222 Gate Generator module is shown as a yellow square pulse (see Figure 4).

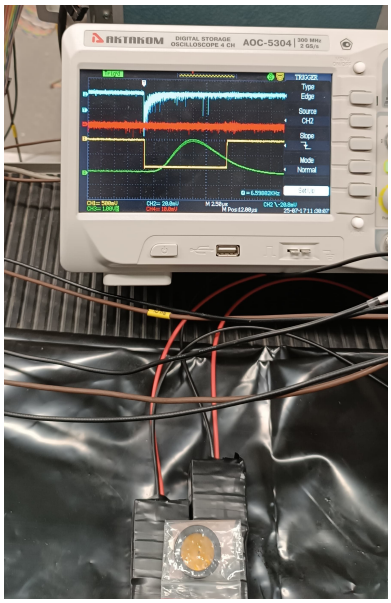

Figure 4: Connection diagram and corresponding signals at different stages of the electronic configuration.

Connection Flow and Functions

1. **PMT → MSCF-16:** Coaxial cable from anode. Amplifies signal (100-1000x) and shapes it into a bipolar pulse optimized for CsI(Tl).
2. **MSCF-16 → TRIVA 7:** Trigger-dead time module.
3. **MSCF-16 → Dual Gate Generator:** CFD output to START input, creating a GATE window μs.
4. **Dual Gate Generator → TRIVA 7:** GATE signal is checked against the dead time of the measurement.

5. **TRIVA 7 → VULOM4B:** Valid event signals for coincidence logic.

6. **VULOM4B → MADC-32:** Common TRIGGER for energy digitization.

7. **MSCF-16 → MADC-32:** This module sends the integrated signal to the digitization unit.

8. **MADC-32 → ENV-3:** This module converts differential GATE signal from VULOM to unipolar GATE signal for MADC-32.

Data Control and Processing: Module control was performed using a computer running the *Multi Branch System* (MBS) developed by the Helmholtz Centre (Germany). This software managed real-time acquisition, including filtering, histogramming, and coincidence analysis via Go4. Data were stored and analyzed in ROOT format.

The hardware included MADC-32, MSCF-16, ENV-3 modules, interconnected via Ethernet. Front-end computers ran specific drivers. The MBS server coordinated data flow, triggers, and module synchronization.

Two measurements were performed, each lasting 30 minutes for the ^{22}Na and ^{60}Co radioactive sources. Data were saved in `.lmd` format and converted to ROOT using Go4 user libraries.

2.2.2 PicoScope 6402D

The PicoScope 6402D is a high-performance digital oscilloscope from Pico Technology's 6000 series, designed for laboratory applications requiring high sampling speed and deep memory capacity. It features a bandwidth of 250 MHz, four analog channels, and a sampling rate of up to 5 GS/s, with a memory depth of 512 Mpts that allows capturing and analyzing waveforms detected by scintillators. Its 8-bit vertical resolution and approximate rise time of 1.4 ns enable reconstruction of fast waveforms. This device connects to a computer via USB 3.0 and is controlled using the PicoScope 6 software [8].

To visualize the signal from the PMT coupled to the CsI(Tl) scintillator, it was only necessary to connect its output to one of the four signal input ports [see Figure 5a]. To control this device, it was connected via a USB cable to a computer with the corresponding software installed [see Figure 5b].

The following parameters were configured in the software: input impedance of 50 Ω, baseline at 180 mV, trigger at 174 mV, time scale of 2 μs/div, and sampling frequency of 5 GS/s.

Thus, when visualizing signals like the one shown in Figure 5b, the information was saved in `.csv` format for subsequent analysis.

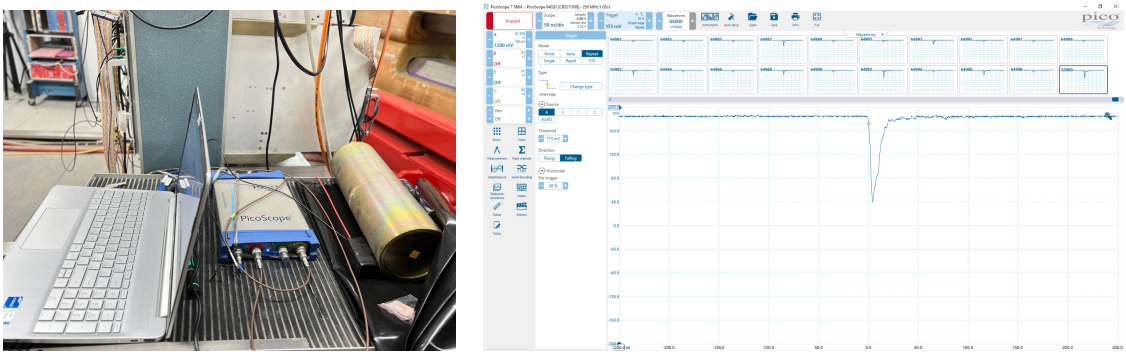

(a) Connecting the Picoscope.

(b) Virtual software environment.

Figure 5: Picoscope oscilloscope and waveform collection.

The measurements performed are shown in Table 2. This includes the BC404 scintillator which operated with a bias voltage of 2275 V at 350 mA.

Table 2: Experimental configuration of the measurements

Scintillator material	Radioactive source (Measurement)	Number of samples
CsI(Tl)	1: ^{22}Na	20k
	2: ^{60}Co	20k
BC404	1: ^{22}Na	30k

The `.csv` files were converted to `ROOT` format through the creation of a C++ code, which is presented in Appendix A. This code also generates a new histogram by calculating, for each event, the integral of the obtained waveform. Since these are discrete steps, the integral was estimated using the numerical trapezoidal method.

3 Results and Analysis

The results of various measurements performed using the MBS acquisition system and the Picoscope are presented and discussed below.

3.1 Measurement of the 1" and 2" CsI(Tl) detectors with MBS system

To generate spectra from radioactive sources using the CsI(Tl) scintillators of 1" and 2", the code presented in Appendix B was developed. This code opens the ROOT file unpacked by Go4 user libraries.

Additionally, using the characteristic peaks of these sources, equation 1.2 was individually fitted, allowing extraction of centroids for linear channel-to-energy calibration. Finally, the code generates the calibrated histograms shown in Figure 6.

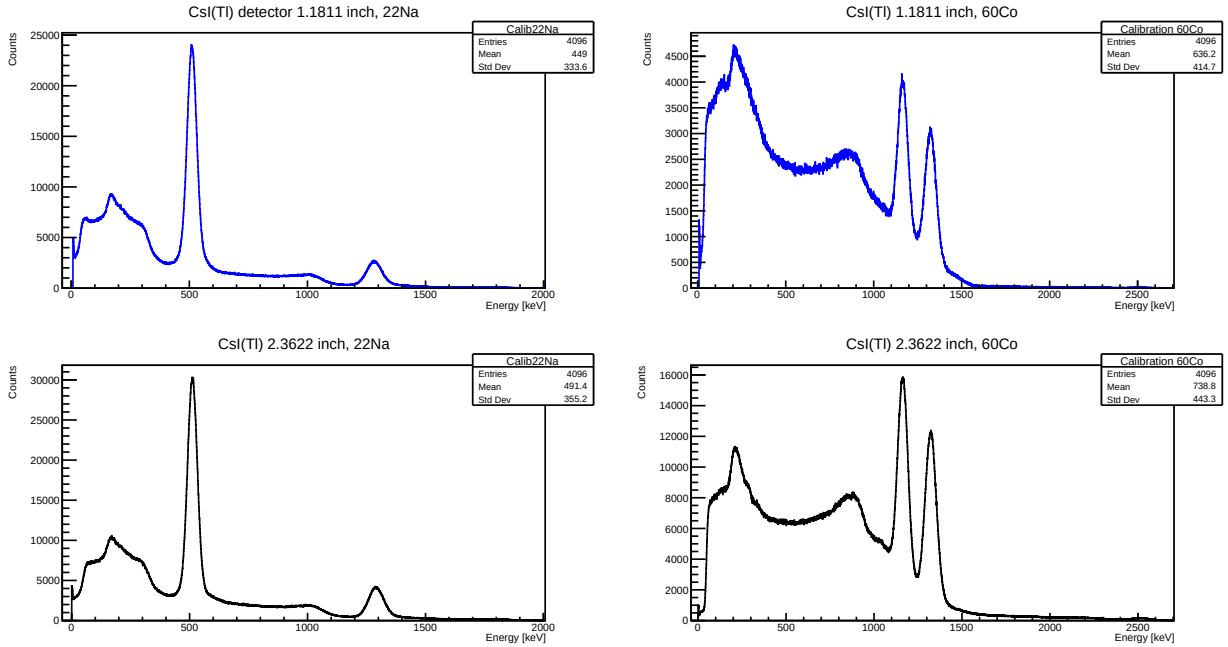

Figure 6: Spectra of radioactive sources with CsI(Tl) detectors of 1" and 2"

The channel-to-energy calibration for both detectors is shown in Figure 7, and the corresponding code can be found in Appendix C. Both linear fits show acceptable quality, with a coefficient of determination $R^2 \approx 0.99$.

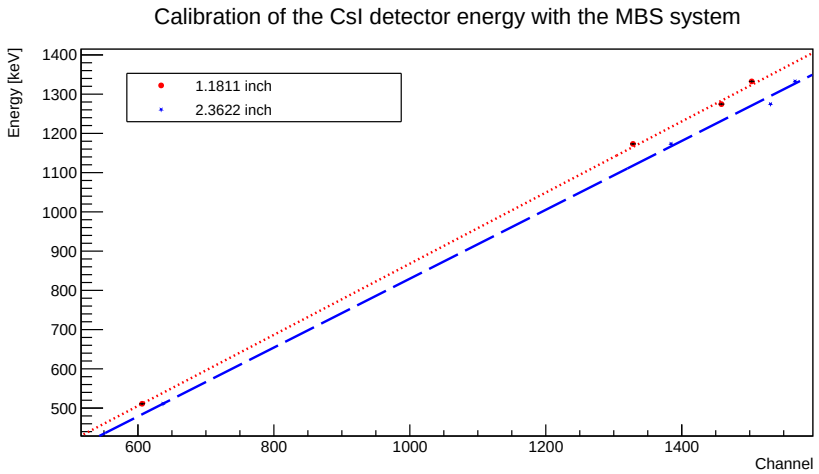

Figure 7: Channel-to-energy calibration for CsI(Tl) scintillators

The resolution parameter obtained using equation 1.4 for the photopeaks of the energy-calibrated spectra is shown in Figure 8.

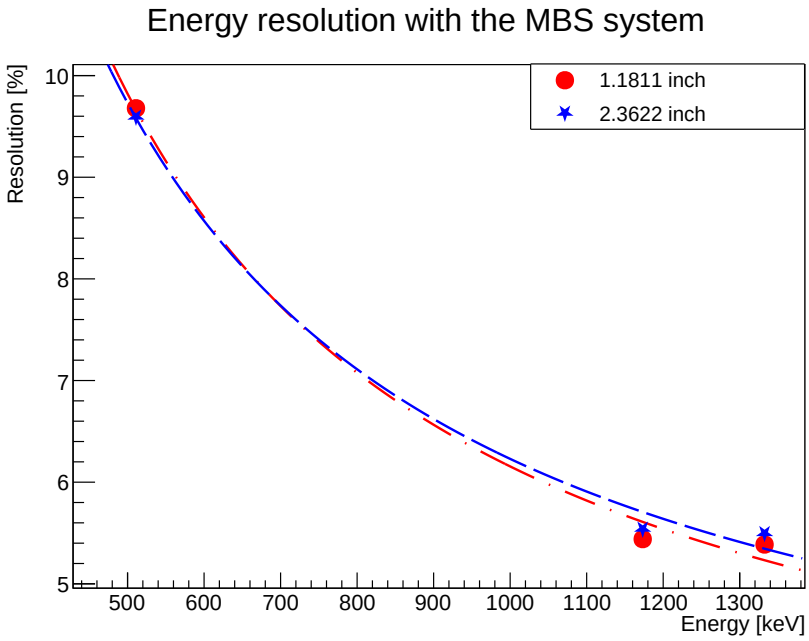

Figure 8: Energy resolution for CsI(Tl) detectors

In the previous graph, a nonlinear fit was performed given by the equation 1.5. The results obtained are presented in table 3.

Detector	Parameter	Value ± Error
1"	A	146.1 ± 7.8
	B	1054.0 ± 155.0
	C	−143.7 ± 7.7
2"	A	146.3 ± 7.7
	B	1029.9 ± 158.2
	C	−143.6 ± 7.7

Table 3: Results of resolution fits for CsI(Tl) detectors

As seen in Figure 6, the energy spectra for each radioactive source and for different dimensions of the detector can be observed. Visually, we can observe the same photopeaks, back scatter peaks and the formation of Compton continuums. However, the spectrum obtained with the 2" detector shows greater definition and less noise.

On the other hand, when analyzing the energy resolution [see Figure 8], a slight difference is noted for energies below 620 keV, where the 2" detector performs slightly better. In the interval between 620 keV $< E <$ 720 keV both detectors show similar behavior, while for energies between 720 keV $< E <$ 1400 keV the 1" detector shows superior resolution.

3.2 Picoscope and MBS results for 1" CsI(Tl) detector

To analyze this spectrum with ROOT, a C++ code similar to that shown in Appendix B was created. Similarly, photopeaks were fitted using equation 1.2 to determine centroids, which were used to calibrate the spectrum. This yielded the calibrated spectra shown in Figure 9.

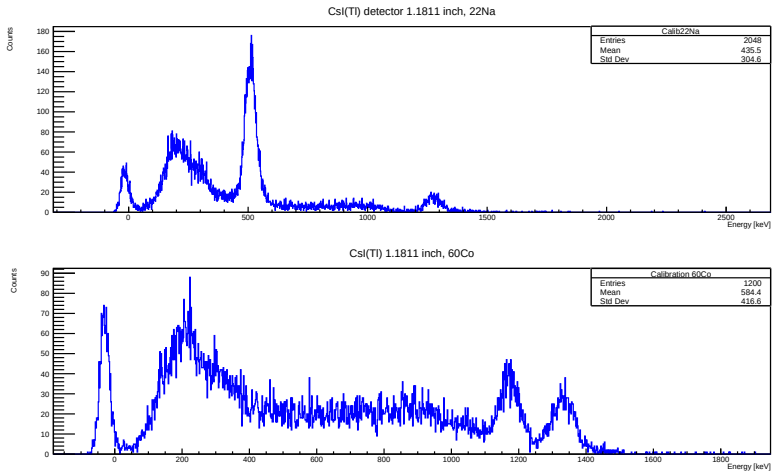

Figure 9: Calibrated spectra obtained with the Picoscope

The code for channel-to-energy calibration was similar to the code in Appendix C. The linear fits are shown in Figure 10, with a coefficient of determination $R^2 \approx 0.999$.

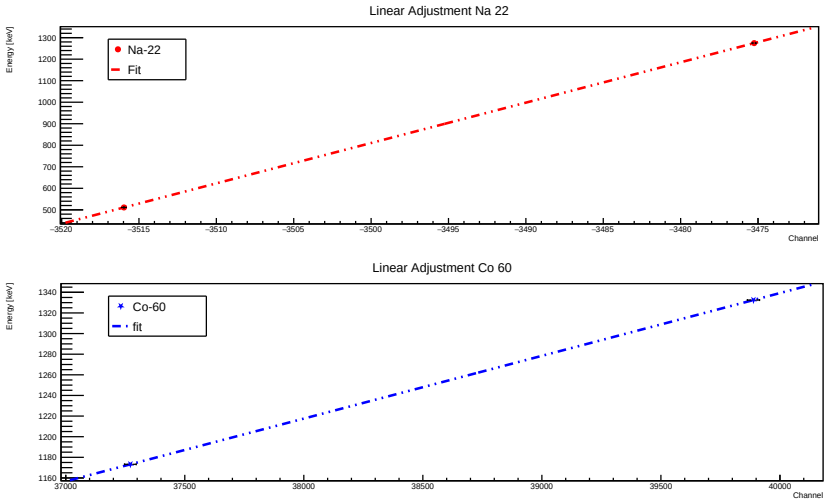

Figure 10: Channel-to-energy calibration for the CsI(Tl) detector using the Picoscope

The energy resolution obtained through this experimental method and computational analysis was compared with that obtained using the MBS system for the same scintillator material and length, as shown in Figure 11.

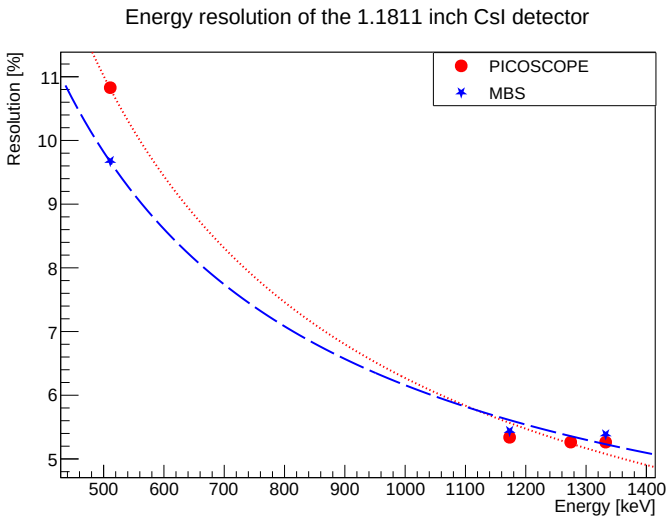

Figure 11: Comparison of energy resolution between the Picoscope and MBS systems

Similarly, equation 1.5 was used for the resolution fit, and the resulting parameters are shown in Table 4. This figure shows the difference in resolution between both systems. While the MBS system performs better for energies below 1000 keV, for 1000 keV $< E <$ 1220 keV, both systems exhibit similar behavior. And for energies above 1220 keV, the Picoscope progressively achieves better resolution as E increases.

System	Parameter	Value ± Error
PICOSCOPE	A	428.6 ± 1.9
	B	2033.3 ± 62.2
	C	−427.2 ± 1.9
MBS	A	146.1 ± 7.7
	B	1054.0 ± 155.0
	C	−143.7 ± 7.7

Table 4: Results of resolution fits for the Picoscope and MBS systems

3.3 Results for the BC404 Detector

For this section, a measurement previously performed by our group using the BC404 detector and the MBS system was compared with the data obtained in this work using the Picoscope for the ^{22}Na source. Due to the properties of the scintillator, it is not possible to fit the spectrum using equation 1.2, as was done for the CsI(Tl) spectra. In this analysis, the energy-related information that was used for energy calibration were the Compton edges, which were determined by fitting the spectra with the Fermi function (see equation 1.3).

The results obtained for the BC404 scintillator, using both the MBS system and the Picoscope, are shown in Figure 12.

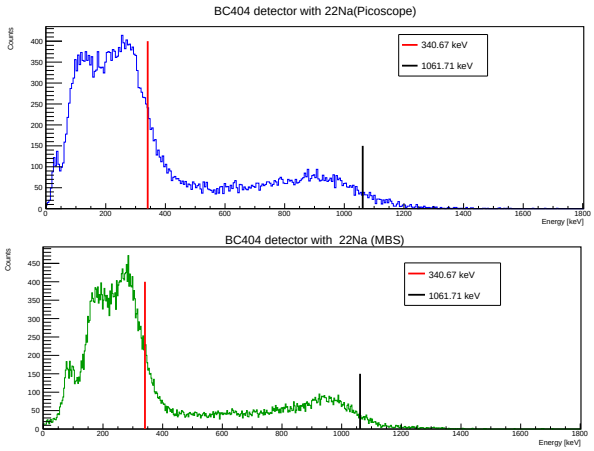

Figure 12: Calibrated spectra of the ^{22}Na source for the BC404 detector with the MBS system and Picoscope

The channel-to-energy calibration for the BC404 scintillator follows the structure of the code in Appendix C, as it also maintains a linear relationship, as shown in Figure 13, with a coefficient of determination $R^2 \approx 0.999$ in both cases.

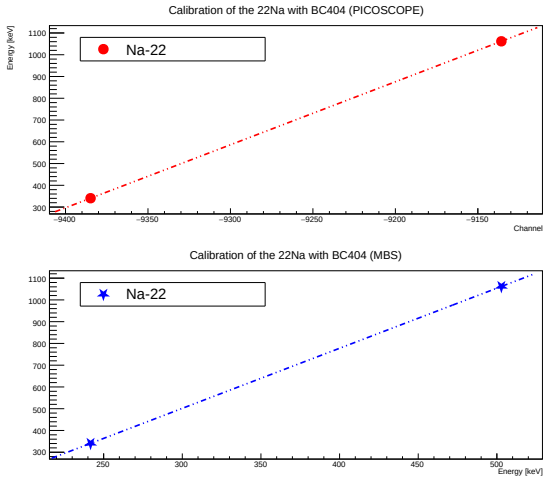

Figure 13: Linear fits for channel-to-energy calibration of the BC404 detector with the MBS system and Picoscope

The data presented in the energy-calibrated spectrum [see Figure 12] for the BC404 scintillator shows that both methods, MBS and Picoscope, are capable of reproducing the same phenomenon. This is evidenced by the defined energies of the Compton edges, 340.67 keV and 1061.71 keV (determined individually), being located at the same positions, and the histograms maintaining the same behavior of the phenomenon.

4 Conclusion

The work presented in this report details a comprehensive experimental development for scintillator detectors, from detector preparation, data collection to data analysis, highlighting the importance of maintaining optimal conditions to ensure data reliability.

In the first part, we addressed the need to minimize measurement noise, achieved by using a homogeneous CsI(Tl) scintillator material, carefully lapped to preserve its optical properties. The coating proved equally relevant, as it preserves the scintillation effect and optimizes coupling with the photomultiplier tube (PMT). Significant differences in refractive indices between materials or the presence of air bubbles can scatter light and affect measurements, causing variations of up to 0.5 units, which are significant for the experiments.

In the second part, we worked with two different CsI(Tl) lengths: 1" inch and 2". The spectra show similar behaviors, provided the values of resolution for the 511 keV and 1372 keV photopeaks. The values are close to one another as expected, since the volume of the scintillator is small with comparison to the light absorption length (about 17 cm), so the efficiency of light transport can be safely neglected.

The computational analysis performed in ROOT for the Multi Branch System (MBS) and Picoscope acquisition systems confirmed similar radiation interactions. The MBS, though more complex to operate due to handling electronic modules and specialized programming, offers better resolution at energies lower than 1 MeV. The Picoscope is simpler to configure, which could be advantageous in measurements with nearby energy peaks, however this method produces spectra with worse resolution at energies below 1 MeV. For example, with a ^{22}Na source, the 511 keV annihilation energy was measured with 10.9% resolution (55.7 keV), while the ^{137}Cs photopeak (661.657 keV) showed 8.7% resolution (57.6 keV). We have found out that at energies > 1 MeV both MBS and waveform analysis perform equally well. However, at lower energies, a more advanced analysis of waveforms is needed.

For the organic BC404 detector, the analysis differed due to the material's properties. Calibration was performed by fitting data with the Fermi equation and extracting Compton edges. In future works, determining the energy resolution of this scintillator will help distinguish some characterizations between organic and inorganic scintillators more precisely.

Finally, this study establishes a solid methodological foundation for research with other scintillators detectors, such as stilbene, a material renowned for its high neutron detection efficiency due to pulse-shape discrimination capabilities, and relevant for studying prominent nuclear reactions in our group.

References

[1] Laboratories, "Joint institute for nuclear research." https://www.jinr.ru/jinr_structure-en/laboratories-en/.

[2] Flerov Laboratory of Nuclear Reactions, "ACULINA facility at FLNR JINR." http://aculina.jinr.ru/index.html, 2023.

[3] Admin, "First experiments at acculinna-2 fragment-separator – flerov laboratory of nuclear reactions." https://flerovlab.jinr.ru/first-experiments-at-acculinna-2-fragment-separator/.

[4] G.F. Knoll, *Radiation Detection and Measurement*, John Wiley & Sons (2010).

[5] W.R. Leo, *Techniques for Nuclear and Particle Physics Experiments: A How-to Approach*, Springer Science & Business Media (2012).

[6] Luxium Solutions, "Bc400, bc404, bc408, bc412, bc416." https://luxiumsolutions.com/radiation-detection-scintillators/plastic-scintillators/bc400-bc404-bc408-bc412-bc416.

[7] GSI Helmholtzzentrum für Schwerionenforschung, "Documents on the multi-branch system (mbs): Release notes, user manuals, hardware and auxiliary documentation." https://www.gsi.de/en/work/research/experiment_electronics/data_processing/data_acquisition/mbs/documents.

[8] Pico Technology, "Pico technology – pc-based oscilloscopes, data loggers rf products." https://www.picotech.com/.